*J. Fluid Mech.* (2024), *vol*. 997, A36, doi:10.1017/jfm.2024.830

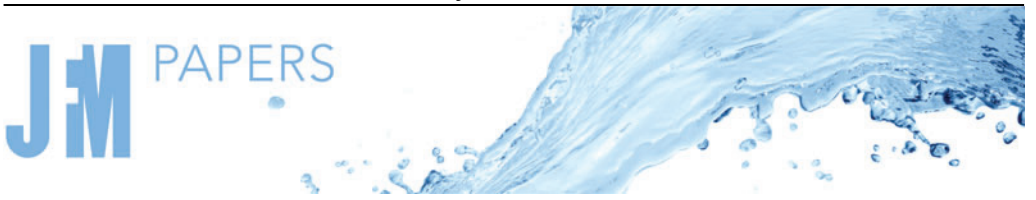

# Free-surface-induced ground effect for flapping swimmers

**Kaiyuan Zheng[1,2], Sida He[3,4], Xizeng Zhao[2], Lian Shen[3,4] and Xiaojue Zhu[1,†]**

[1]Max Planck Institute for Solar System Research, 37077 Göttingen, Germany

[2]Ocean College, Zhejiang University, Zhoushan, Zhejiang 316021, PR China

[3]Saint Anthony Falls Laboratory, University of Minnesota, 2 Third Avenue SE, Minneapolis, MN 55414, USA

[4]Department of Mechanical Engineering, University of Minnesota, Minneapolis, MN 55455, USA

(Received 21 August 2023; revised 2 August 2024; accepted 27 August 2024)

Numerous flying and swimming creatures use the ground effect to boost their propulsive performance, with the 'ground' referring to either a solid boundary or a free surface. While our knowledge of how a solid boundary affects biolocomotion is relatively comprehensive, the ground effect of a free surface is not fully understood. To address this limitation, we conduct a numerical investigation on the propulsion performance of a flapping plate under a free surface, subject to a range of control parameters. When the Froude number ($Fr$) is very low (i.e. little surface deformation), the effects of a free surface are similar to those of a solid boundary, with enhanced thrust and input power but little change in efficiency. However, as $Fr$ increases (i.e. more surface deformation), our results reveal an optimal $Fr$ of approximately 0.6, where the free surface induces a more streamlined flow around the flapping plate, effectively reducing the added mass. This results in a significant decrease in input power and greatly enhanced efficiency.

**Key words:** swimming/flying, propulsion

## 1. Introduction

Historically, the ground effect, which refers to increased lift-to-drag ratios experienced by fixed-wing aircraft near a fixed surface, has been widely studied (Coulliette & Plotkin 1996; Rozhdestvensky 2006). In nature, unsteady flapping swimmers also take advantage of the ground effect to improve their locomotion performance (Blake 1983; Webb 1993,

† Email address for correspondence: zhux@mps.mpg.de

© The Author(s), 2024. Published by Cambridge University Press. This is an Open Access article, distributed under the terms of the Creative Commons Attribution licence (http://creativecommons.org/licenses/by/4.0), which permits unrestricted re-use, distribution and reproduction, provided the original article is properly cited.



https://doi.org/10.1017/jfm.2024.830 Published online by Cambridge University Press

2002; Park & Choi 2010; Blevins & Lauder 2013; Ryu *et al.* 2016). For instance, bacteria swim close to solid surfaces (Berke *et al.* 2008), steelhead trout (Webb 1993), mandarin fish (Blake 1979) and batoids and flatfishes (Quinn, Lauder & Smits 2014*a*) spend a significant amount of time near solid boundaries, while gliding pelicans (Stokes & Lucas 2021), flying fish (Davenport 1994) and swordfish (Lee *et al.* 2009) prefer to swim/fly near the (free) water surface. In the realm of biolocomotion, 'ground' can be categorised into solid boundaries and free surfaces. In recent years, numerous studies (Gao & Lu 2008; Tang *et al.* 2016; Zhong *et al.* 2021; Aju *et al.* 2022) have investigated the impact of solid boundaries on the thrust and efficiency of unsteady flapping swimmers. Experimental and numerical simulations have demonstrated that both rigid and flexible flapping bodies can benefit from enhanced thrust while maintaining almost the same efficiency close to solid boundaries (Quinn *et al.* 2014*a*,*b*; Mivehchi, Dahl & Licht 2016).

The physical mechanisms of performance enhancement arising from the presence of a solid boundary are attributed to two factors, namely the added mass and the circulatory effect (Brennen 1982; Mivehchi *et al.* 2021). The scaling laws derived by Mivehchi *et al.* (2021) indicate that as the distance to the ground decreases, there is an increase in the added mass and a decrease in the influence of shed vortices. Both variations play a crucial role in the enhanced thrust and input power.

In contrast to the above understanding of solid boundaries, the ground effect originating from free surfaces is not yet fully understood. Understanding the unsteady ground effect of free surfaces would not only elucidate the performance of swimmers in nature but also help improve the design of unsteady underwater propulsors that can efficiently swim near the water surface, taking into account the possible ground effect. Several recent investigations have explored the influence of a free surface on flapping bodies, particularly emphasising energy harvesting. For example, Bandyopadhyay (2002) conducted experiments examining the impact of pectoral wings on manoeuvring and station-keeping in the presence of oncoming surface waves. In this context, the Froude number is employed as a method to attain high manoeuvrability, independent of the deformation of the free surface. Filippas & Belibassakis (2014) explored oscillating wings as dynamic thrusters, enhancing a ship's overall propulsion in wave conditions. The heave motion of the flapping propulsor is initiated by the ship's movements, while the pitching motion is controlled actively. In the presence of waves, the thrust coefficient is noted to significantly surpass its value in an infinite domain, with a maximum gain reaching 20 %. Unlike the investigation conducted by Filippas & Belibassakis (2014), Deng *et al.* (2022) proposed that the free surface has a detrimental impact on the efficiency of energy harvesting through lift force and pitching moment. A similar conclusion has also been drawn by Zhu *et al.* (2022). Notably, Chung (2016) was the first who examined the thrust and propulsive efficiency of a flapping plate near an otherwise quiescent free surface, but due to limitations in the parameter space studied (only one Reynolds number and two Froude numbers were considered), the biological implications remain unclear.

The goal of this study is to systematically investigate the impact of a free surface on the propulsive performance of a flapping plate through numerical simulations, focusing on the Froude number dependence and Reynolds number dependence. The key findings of this study include the following: (*a*) a free surface also induces a ground effect, but unlike the ground effect resulting from a solid boundary where the efficiency of the flapping body remains relatively constant, the free surface can greatly reduce the required input power, leading to significantly higher swimming efficiency; and (*b*) there exists an optimal Froude number of approximately 0.6, where the efficiency enhancement is at its maximum.



https://doi.org/10.1017/jfm.2024.830 Published online by Cambridge University Press

## 2. Physical model and numerical settings

A sketch of the numerical model is shown in figure 1. A flapping plate, which mimics the motion of an unsteady swimmer, is heaved and pitched harmonically at the leading edge while subject to an incoming flow (Chung 2016). The governing equations for the fluid motion are the two-phase, incompressible Navier–Stokes equations (Calderer *et al.* 2018; He *et al.* 2022):

$$\nabla \cdot \boldsymbol{u} = 0, \tag{2.1}$$

$$\frac{\partial \boldsymbol{u}}{\partial t} + \boldsymbol{u} \cdot \nabla \boldsymbol{u} = \frac{1}{\rho(\phi)} \left[ -\nabla p + \nabla \cdot (\mu(\phi) \boldsymbol{S}) + \rho(\phi) \boldsymbol{g} \right] + \boldsymbol{f}, \tag{2.2}$$

where $\boldsymbol{u}$ represents the velocity, $\rho(\phi)$ is the fluid density, $p$ is the pressure, $\mu(\phi)$ is the dynamic viscosity, $\boldsymbol{S} = (\nabla \boldsymbol{u} + \nabla \boldsymbol{u}^{\mathrm{T}})/2$ is the strain rate tensor, $\boldsymbol{g}$ is the gravitational acceleration and $\boldsymbol{f}$ is the force exerted by the flapping plate on the fluid. Note that $\rho(\phi)$ and $\mu(\phi)$ are fluid-phase-dependent (see figure 1). In our simulations, $\rho_1/\rho_2$ and $\mu_1/\mu_2$ are fixed at $1.226 \times 10^{-3}$ and $1.565 \times 10^{-2}$, respectively, to reflect the difference between water and air. The flapping motion of the plate is prescribed as $y_h(t) = h_1 \sin(2\pi f t)$ and $\alpha(t) = \alpha_1 \sin(2\pi f t + \delta)$, where $y_h(t)$ is the instantaneous heaving position, $h_1$ is the amplitude of heaving motion, $f$ is the frequency, $\alpha(t)$ is the instantaneous pitch angle, $\alpha_1$ is the amplitude of pitching motion and $\delta$ is the phase angle. If choosing the incoming flow velocity $U_\infty$ as the characteristic velocity scale and the plate chord length $C$ as the characteristic length scale, several important dimensionless parameters arise, namely:

$$\left.\begin{gathered} \bar{A} = \frac{2A}{C}, \quad \bar{H} = \frac{H_0}{C}, \\ Re = \frac{\rho_2 U_\infty C}{\mu_2}, \quad St = \frac{2fA}{U_\infty}, \quad Fr = \frac{U_\infty}{\sqrt{gC}}, \end{gathered}\right\} \tag{2.3}$$

which are the dimensionless peak-to-peak amplitude ($A$ is the cumulative amplitude of the coupled motion), dimensionless submergence depth ($H_0$ is the depth of the plate leading edge from the free surface), Reynolds number, Strouhal number and Froude number, respectively. Because we have set the characteristic velocity scale and length scale to be the incoming velocity and chord length, respectively, the dimensionless $U$ and $L$ in the simulations have unit values by definition. Therefore, cases with different $Re$ are the equivalent of having different normalised numerical $\mu_2/\rho_2$. Similarly, different $Fr$ and $St$ correspond to different normalised numerical $g$ and $f$, respectively. In contrast to the scenario where no free surface is present, the Froude number $Fr$ is now an important parameter that determines how deformable the free surface is. The fluid–structure interaction in the simulation is achieved by an external-forcing immersed boundary method (He *et al.* 2022), while the free surface is captured by the coupled level set and volume-of-fluid method (Sussman & Puckett 2000). The latter method utilises an interface reconstruction algorithm, which accurately captures the nonlinear evolution of the free surface while ensuring mass conservation. The integrated solver has been tested and benchmarked extensively (Yang, Deng & Shen 2018; Gao, Deane & Shen 2021; He *et al.* 2022) for two-phase flows coupled with fluid–structure interaction.

## 3. Free-surface-induced ground effect at $Re = 200$

The values of the physical parameters used in this section are listed in table 1. In the simulations, $Re = 200$, $h_1 = 0.25$, $\alpha_1 = 15^\circ$, $\delta = -\pi/2$ and $W = C/20$ (thickness of the



https://doi.org/10.1017/jfm.2024.830 Published online by Cambridge University Press

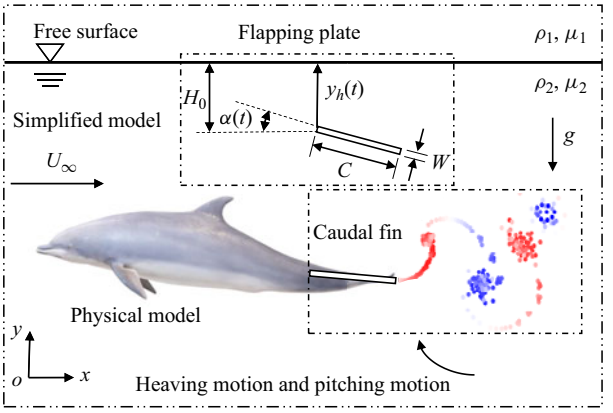


Figure 1. Schematic diagram illustrating the unsteady propulsion of a flapping plate in the vicinity of a free surface. Aquatic animals such as dolphins and flying fish often approach the water surface before gliding or taking off, but the mechanisms by which they utilise the free surface to enhance their propulsive efficiency over long distances remain unclear (Deng *et al.* 2019). Here, $\rho_2$, $U_\infty$ and $C$ are chosen as the characteristic density, velocity and length, respectively. All other physical quantities are made dimensionless using these parameters. In the simulations, the caudal fin region is simplified into a flapping plate and the animal body part is not considered.

| $Fr$ | $St$ | $\bar{H}$ |
|---|---|---|
| 0.2 | 0.3, 0.45 and 0.6 | [0.5, 5.0] |
| 0.4 | 0.3, 0.45 and 0.6 | [0.3, 5.0] |
| 0.6 | 0.3, 0.45 and 0.6 | [0.3, 5.0] |
| 0.8 | 0.3, 0.45 and 0.6 | [0.3, 5.0] |

Table 1. Control parameters adopted in the simulations. Four $Fr$ and three $St$ values are chosen, while the dimensionless submergence depths $\bar{H}$ vary from very close to very far from the free surface.

plate). A similar prescribed motion has been adopted in many previous studies for flapping swimmers (Li & Lu 2012; Wu *et al.* 2015; Chung 2016), modelling the effect of caudal fin and cetacean-like swimmers. For generality, we vary $Fr$, $St$ and $\bar{H}$, resulting in a total of 102 simulations. Throughout the simulations, we ensure that the flapping plate did not come into contact with the free surface. The collected data were then averaged over 40 cycles after achieving a statistically stationary state.

We begin by illustrating the effects of a free surface on the flow structure, as depicted in figure 2. When $Fr$ is low, i.e. 0.2, the surface deformation is negligible, and the vortex dynamics is similar to that observed in the presence of a solid boundary (Li & Lu 2012), wherein the negative and positive vortices tend to approach each other and create dipoles that deflect away from the boundary. The surface wave does not synchronise with the motion of the flapping plate, i.e. the gap distance between the free surface and the plate varies non-uniformly. As $Fr$ increases to 0.6, the surface deformation becomes significant, and the gap distance between the surface and the plate remains relatively constant along the gap, giving rise to a streamlined surface wave. Simultaneously, the wake moves straight downstream, with no further deflection. As $Fr$ increases to 0.8, the surface deformation becomes more pronounced, and the wake behind the flapping plate loses its coherence. At some instances, localised surface sharpening and breaking can be observed. Note that



https://doi.org/10.1017/jfm.2024.830 Published online by Cambridge University Press

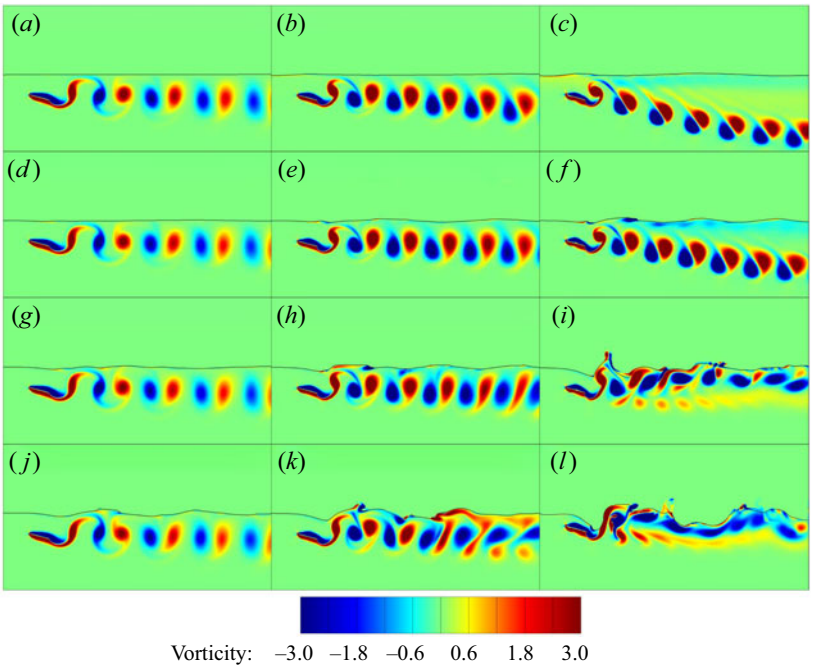


Figure 2. Instantaneous free surface and vortex structure snapshots with $\bar{H} = 0.5$: (*a–c*) $Fr = 0.2$, (*d–f*) $Fr = 0.4$, (*g–i*) $Fr = 0.6$ and (*j–l*) $Fr = 0.8$; (*a*,*d*,*g*,*j*) $St = 0.3$, (*b*,*e*,*h*,*k*) $St = 0.45$ and (*c*,*f*,*i*,*l*) $St = 0.6$. All the contour plots are at the same time instant $t = 0.0T$, where $T$ is the cycle time.

the large deformation (curvature) of the free surface, not just the flapping of the plate, generates vorticities. Furthermore, at low $Fr$, surface waves propagate both upstream and downstream, whereas at high $Fr$, surface waves move downstream only. This phenomenon is explained in the following section, in conjunction with figure 4(*b*). Another noteworthy finding is that when $St = 0.3$, the flow structure is affected less by the surface deformation. However, for $St = 0.45$ and $St = 0.6$, the impact of surface deformation on the flow structure becomes more evident.

In the following analysis, we systematically examine how the free surface impacts propulsion performance. Three crucial performance metrics have been established, namely the time-averaged thrust force coefficient $C_T$, the time-averaged input power coefficient $C_P$ and the efficiency $\eta = C_T/C_P$. Coefficients $C_T$ and $C_P$ are defined as

$$C_T = \frac{2\left\langle \oint_S f_x \,\mathrm{d}s \right\rangle}{\rho_2 U_\infty^2 \mathcal{C}}, \quad C_P = \frac{2\left\langle \oint_S \boldsymbol{f}\cdot\boldsymbol{u} \,\mathrm{d}s \right\rangle}{\rho_2 U_\infty^3 \mathcal{C}}, \tag{3.1a,b}$$

respectively, where $f_x$ represents the horizontal component of the fluid–structure interaction force $\boldsymbol{f}$. Two intriguing phenomena can be observed in figure 3. First, at $St = 0.3$, there is no net thrust, and swimming closer to the surface results in a transition from drag to thrust for all $Fr$. However, as the surface deformation increases (higher $Fr$), this transition can occur only by swimming very close to the boundary. Thus, we conclude that the deformation of the free surface alone does not facilitate the drag-to-thrust transition. Second, in contrast, at a higher $St = 0.45$ and $St = 0.6$, there is a net thrust. When $Fr = 0.2$, the free-surface deformation is minimal, and if the plate moves closer to the boundary, the thrust initially increases, accompanied by an increase in the input



https://doi.org/10.1017/jfm.2024.830 Published online by Cambridge University Press

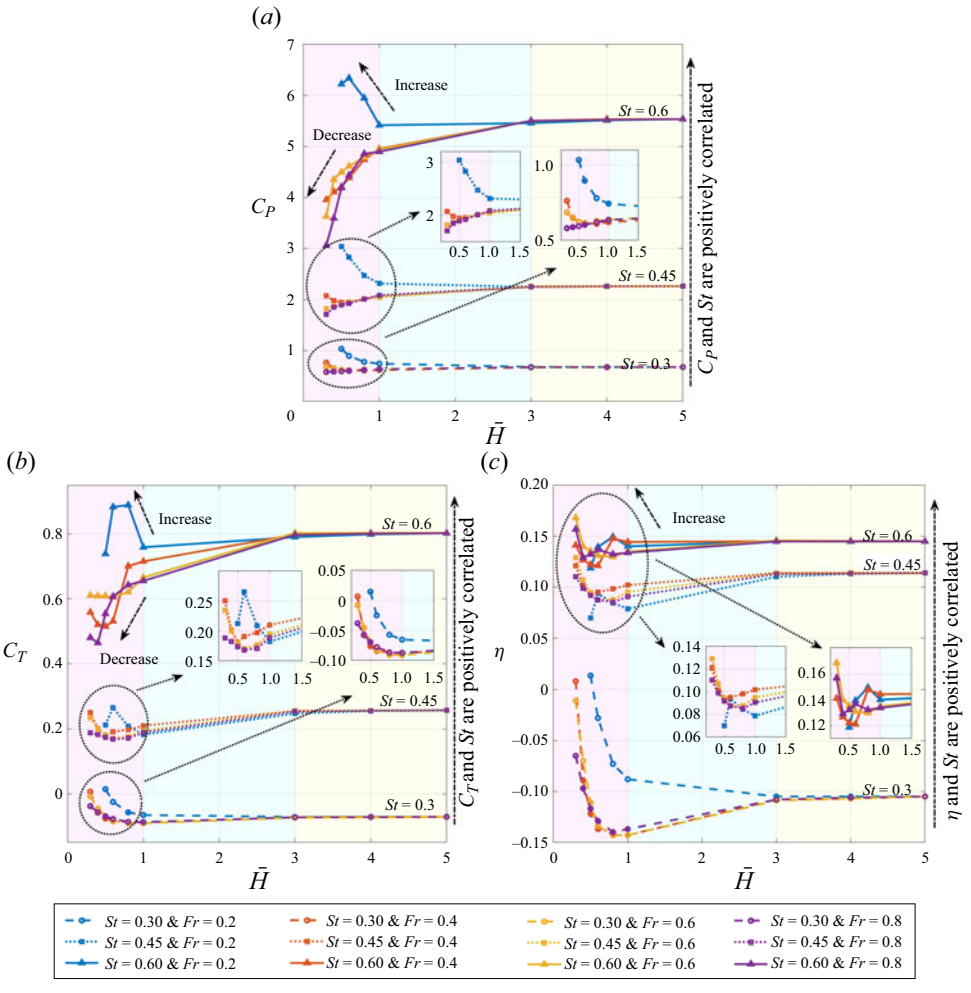


Figure 3. (*a*) Power input coefficient $C_P$, (*b*) thrust coefficient $C_T$ and (*c*) efficiency $\eta$ as a function of the dimensionless submergence depth $\bar{H}$. The simulations reveal three distinct regimes: a significant-ground-effect regime (pink) for $\bar{H} < 1$, a minor-ground-effect regime (blue) for $1 < \bar{H} < 3$ and a no-ground-effect regime (yellow) for $\bar{H} > 3$. There is an optimal propulsive efficiency when the Froude number $Fr = 0.6$ and when there is net thrust in the system.

power (Dai, He & Zhang 2016). This leads to a relatively constant or slightly decreasing efficiency, similar to the effects observed with a solid boundary (Quinn *et al.* 2014*b*). Interestingly, with the same flapping motion, as *Fr* increases, the required input power and induced thrust both decrease, resulting in higher efficiency than in cases where the plate is far away or *Fr* is small. Furthermore, the propulsive efficiency is notably maximised at an optimal Froude number of $Fr = 0.6$.

To explain the performance enhancement and the existence of an optimal *Fr*, we first examine the flow structure illustrated in figure 2. As stated above, when the free surface undergoes deformation, a streamlined flow is induced around the flapping plate. However, we do not anticipate resonance between the free surface and the flapping plate due to the streamlined shape. Such resonance could cause more energy to accumulate in the surface waves, necessitating more input power. To support this claim, we present figure 4, which displays the frequency and propagation direction of the dominant surface waves associated



https://doi.org/10.1017/jfm.2024.830 Published online by Cambridge University Press

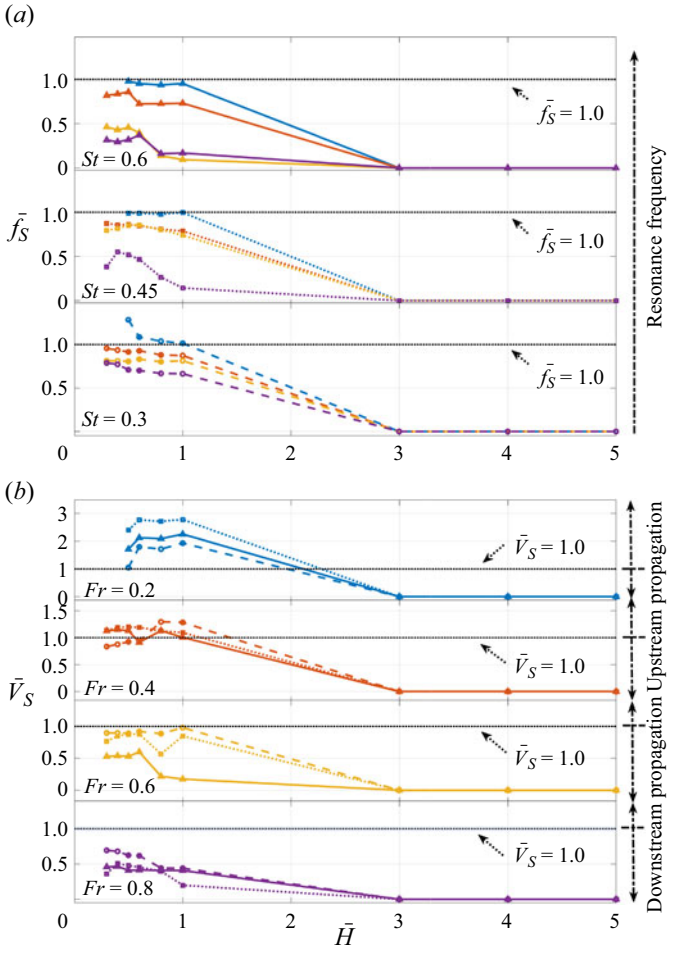


Figure 4. Frequency and propagation velocity of the induced surface waves. (*a*) The dimensionless frequency $\overline{f_S}$. When *St* is 0.3, all cases exhibit close to the plate motion frequency. When *St* is 0.45 and 0.6, at the optimal *Fr*, the system lies away from resonance. (*b*) The dimensionless propagation velocity $\overline{V_S}$. When *Fr* is 0.2, the free-surface wave can propagate both upstream and downstream. When *Fr* is 0.4, the wave can propagate slightly upstream and mostly downstream. When *Fr* is 0.6 and 0.8, the wave can travel only downstream. The line colours and patterns are the same as those in figure 3.

with free-surface deformation. We define the dimensionless frequency as $\overline{f_S} = f_S/f$ and the dimensionless propagation velocity as $\overline{V_S} = V_S/U_\infty$. The frequency $f_S$ and the propagation velocity $V_S$ are obtained by analysing the spatial and temporal data of the surface elevation based on the Fourier transform.

Figure 4 illustrates a comparison of the frequency between the flapping plate and the induced surface wave, as well as the propagation velocity of the surface wave. At the small *Fr* value ($Fr = 0.2$), the frequency of the free surface matches that of the flapping plate, resulting in resonance between them. As a result, the surface waves absorb a significant amount of energy from the fluid. However, as *Fr* increases, the system moves away from resonance, and at the optimal $Fr = 0.6$, the frequency ratio between the surface and plate ranges from 0.5 to 0.8; therefore, no resonance occurs at all. The presence or absence of resonance can also impact the propagation velocity of the surface waves, as presented in



https://doi.org/10.1017/jfm.2024.830 Published online by Cambridge University Press

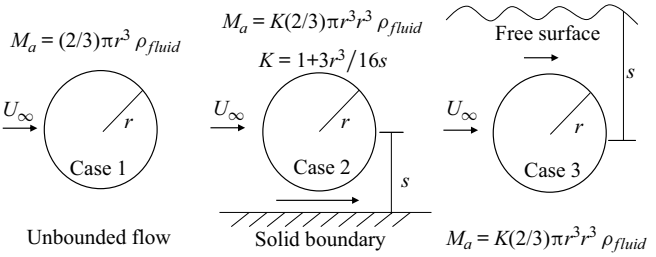


Figure 5. Schematic diagram of the added mass $M_a$ under various conditions. Here, we show an example of a sphere for which there exist exact relations (Brennen 1982); $r$ is the radius of the sphere, $s$ is the distance from the centre of the sphere to the boundary, $\rho_{fluid}$ is the liquid density and $K$ is the added mass coefficient. When the sphere is close to the free surface, $K$ can be reduced to 0.5.

figure 4(*b*). At $Fr = 0.2$, the wave speed is much faster than the incoming flow, and the wave propagates both upstream and downstream. However, at higher $Fr$ values, the wave speed becomes much smaller, requiring less energy to transport. Furthermore, because the wave speed is slower than the incoming flow, the surface waves can propagate only downstream, i.e. not upstream.

Another important factor to consider is the impact of added mass in different scenarios. The added mass stems from the kinetic energy added to a fluid by an object moving in an unsteady manner. In reality, the object's influence extends throughout the entire fluid, not limited to a specific region around the boundary. However, despite this broader influence, the concept of added mass remains invaluable in elucidating fundamental flow physics for objects moving in viscous flow (Fernando, Weymouth & Rival 2020; Reijtenbagh, Tummers & Westerweel 2023). Figure 5 provides an illustration of the added mass in three distinct cases: a sphere positioned far from a boundary, a sphere positioned near a solid boundary and a sphere positioned close to a free surface (Brennen 1982). Here we only show the sphere cases because for sphere cases there exist exact solutions, even for spheres close to a solid boundary (Brennen 1982). When swimming in close proximity to a solid boundary (or at low $Fr$), the added mass tends to increase as the fluid between the boundary and the body accelerates. Consequently, to maintain the same movement, both the input power and the thrust need to increase. This concept of increased added mass from Brennen (1982) has been used to elucidate the scaling of lift or drag for a flapping foil near a solid boundary (Mivehchi *et al.* 2021; Han *et al.* 2024). In contrast, with a free surface, the streamlined shape of the surface allows it to follow the shape of the body, leading to less fluid acceleration between the free surface and the body. As a result, the added mass for the free surface case can be smaller than for the case where the sphere is far from the boundary. A decrease in the added mass leads to a reduction in the required power input and an increase in efficiency. Now we could also explain why there is an optimal $Fr$ and why the $Fr$ effect is not monotonic. When $Fr$ is very small, the free surface has negligible impact, resembling a solid boundary. On the other hand, at high $Fr$, significant surface deformation may occur, potentially leading to the breakup of the surface waves, which is also undesirable in performance. The added mass effect is shown in figure 6, which illustrates the horizontal and vertical velocities around the plate and in the wake region. We observe a decrease in the kinetic energy associated with the perturbed fluid within the computational domain as the Froude number increases (both horizontal and vertical velocities decrease with increasing $Fr$). Excessive $Fr$ values may lead to surface breakup, resulting in enhanced energy consumption, highlighting the existence of an optimal $Fr$.



https://doi.org/10.1017/jfm.2024.830 Published online by Cambridge University Press

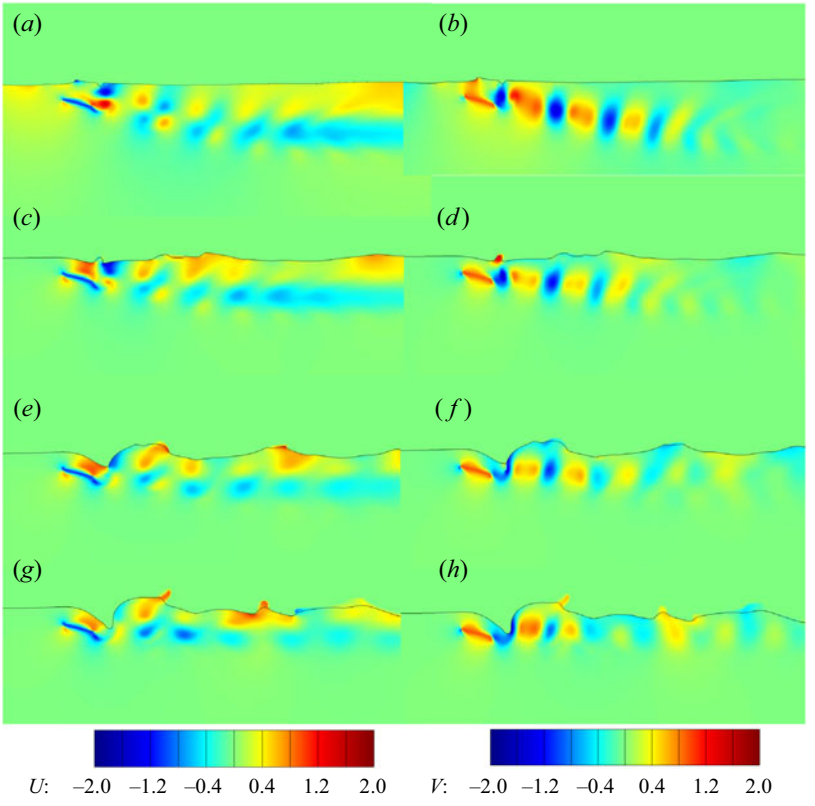


Figure 6. Instantaneous free surface and velocity component snapshots with $\bar{H} = 0.5$ and $St = 0.45$: (*a*,*b*) $Fr = 0.2$, (*c*,*d*) $Fr = 0.4$, (*e*,*f*) $Fr = 0.6$ and (*g*,*h*) $Fr = 0.8$; (*a*,*c*,*e*,*g*) velocity component $U$ and (*b*,*d*,*f*,*h*) velocity component $V$.

Another effect worth noticing is that when $\bar{H}$ decreases from 3 to 1 (see figure 3), the initial decrease in thrust occurs because, at a greater distance from the free surface, the free surface effectively behaves like a solid boundary. As a result, the added mass increases, leading to a reduction in thrust. The reduction in added mass occurs only when the plate is sufficiently close to the free surface, causing deformation and minimising the added mass. This phenomenon is again consistent with the findings by Brennen (1982), where he demonstrated that even a sphere approaching the free surface experiences an initial increase followed by a subsequent decrease in added mass.

## 4. Local dynamics

To better illustrate how the local free-surface deformation varies in relation to the kinematics of the flapping plate, figure 7 shows the instantaneous shape of the free surface at two distinct time instants: one when the plate is moving upward (figure 7 top panels) and one when the plate is moving downward (figure 7 bottom panels). When the plate is moving upward, the surface deformation is minimal for the $Fr = 0.2$ case. In contrast, for $Fr = 0.6$ and $Fr = 0.8$, the surface deformation closely follows the kinematics of the flapping plate. Notably, for $Fr = 0.8$, the surface shape changes drastically behind the plate, forming a cliff-like structure, especially for larger $St$. A similar pattern is observed when the plate is moving downward.



https://doi.org/10.1017/jfm.2024.830 Published online by Cambridge University Press

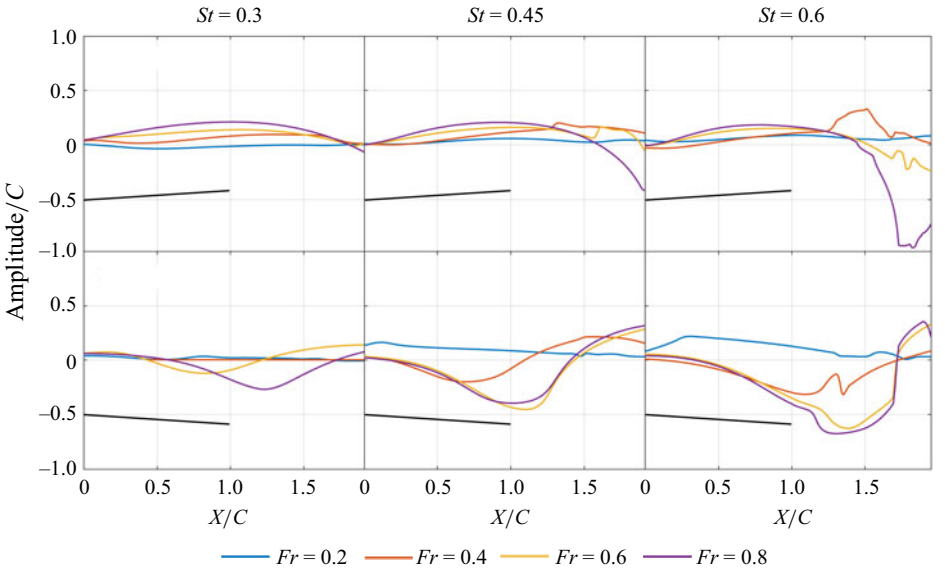


Figure 7. Instantaneous free-surface deformation near the flapping plate for various $Fr$ values, all with a consistent depth of $\bar{H} = 0.5$. The solid black lines represent the position of the flapping plate, while the coloured lines depict the instantaneous positions of the water–air interfaces at different $Fr$.

The effect of local surface deformation dynamics is also reflected in the thrust and input power throughout one cycle. In figure 8, we present the instantaneous thrust force and input power over one cycle for different cases. Higher $St$ leads to higher instantaneous thrust and input power. Notably, in the first half-cycle, where the plate moves downward from its initial position and then upward, and in the second half-cycle, where the plate first moves upward and then downward, the $Fr = 0.2$ case shows almost the same thrust but significantly different input power. In contrast, for other $Fr$ values, the thrust varies considerably between the two half-cycles, while the input power remains quite similar. This suggests that when surface deformation is minimal, the instantaneous input power can increase significantly as the plate moves closer to the surface due to the acceleration of fluids between the plate and the non-deformable surface, as previously noted. For higher $Fr$ values, however, the surface deformation is closely linked to the kinematics of the flapping plate, resulting in much smaller differences in input power between the two cycles, especially for $Fr = 0.6$ and $Fr = 0.8$. On the other hand, thrust generation is not significantly associated with streamlined surface deformation.

## 5. Reynolds number dependence

This section is dedicated to enhancing our comprehension of the $Re$ dependence. Here we focus on cases with $Re = 400$ and $Re = 600$, and we maintain fixed values of $Fr = 0.6$ and $St = 0.45$ while varying $\bar{H}$.

Snapshots capturing the instantaneous free surface and vortex structures at $Re = 400$ and $Re = 600$ are illustrated in figure 9. A comparative analysis unveils both similarities and distinctions when compared with $Re = 200$. The overall flow structure remains akin to that of the $Re = 200$ scenario, where the wake is deflected downward when the plate is away from the surface ($\bar{H} > 1$), resembling cases with a solid boundary (Quinn *et al.* 2014*b*). As the plate approaches the surface, the wake deflection diminishes. However, a



https://doi.org/10.1017/jfm.2024.830 Published online by Cambridge University Press

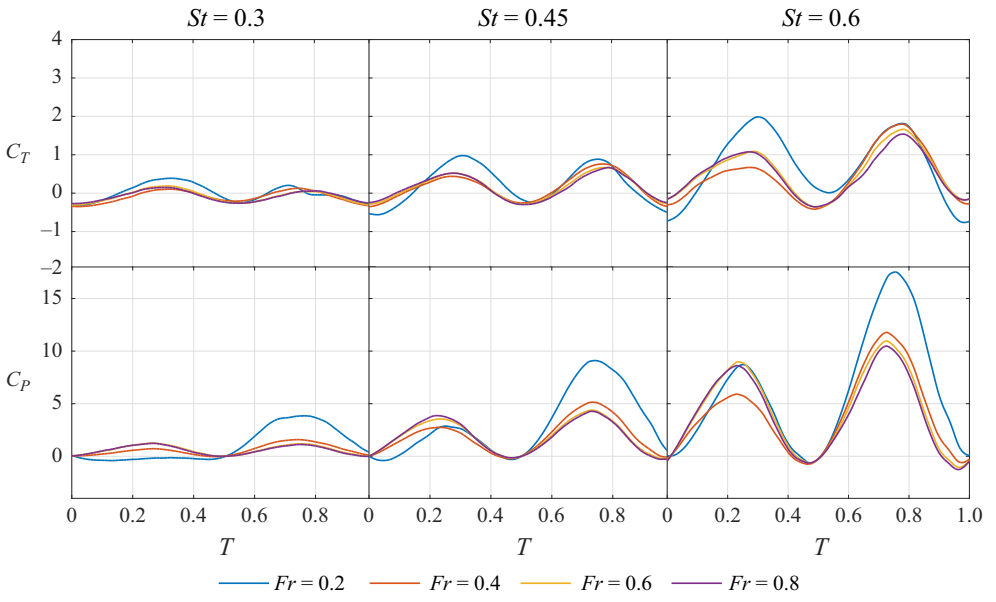


Figure 8. Instantaneous thrust force $C_T$ and input power $C_P$ for various $Fr$ values, all at a constant depth of $\bar{H} = 0.5$. In the first half-cycle, the plate moves downward from its initial position and then upward. In the second half-cycle, the plate moves upward and then downward.

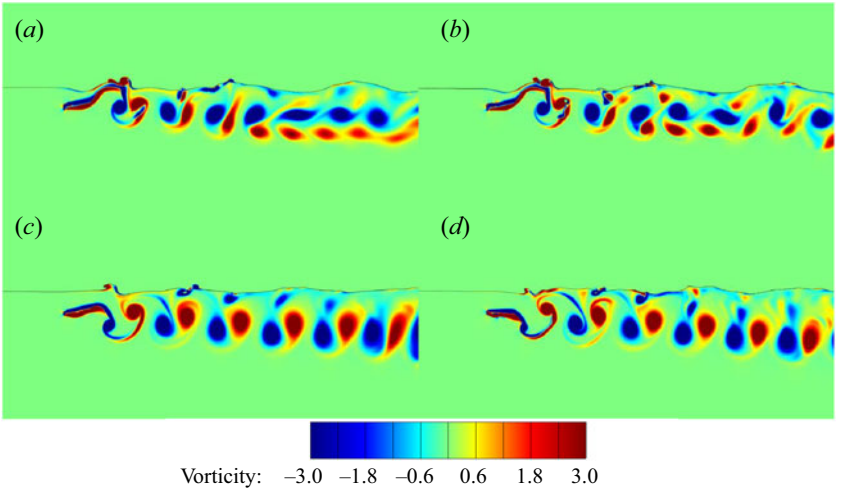


Figure 9. Instantaneous free surface and vortex structure snapshots for $Re = 400$ and $Re = 600$: ($a$,$c$) $Re = 400$ and ($b$,$d$) $Re = 600$; ($a$,$b$) $\bar{H} = 0.6$ and ($c$,$d$) $\bar{H} = 1.0$. For all cases, $Fr = 0.6$ and $St = 0.45$.

notable difference at higher $Re$ is the emergence of high-curvature regions around the surface and the generation of small vortices near these areas, leading to an increased likelihood of surface breakups.

Figure 10 depicts the power input coefficient $C_P$, thrust coefficient $C_T$ and efficiency $\eta$ in relation to the dimensionless submergence depth $\bar{H}$ for $Re = 400$ and $Re = 600$. The outcomes again closely resemble those for $Re = 200$. Specifically, there is a trend of decreasing input power and increasing thrust as the flapping plate approaches the



https://doi.org/10.1017/jfm.2024.830 Published online by Cambridge University Press

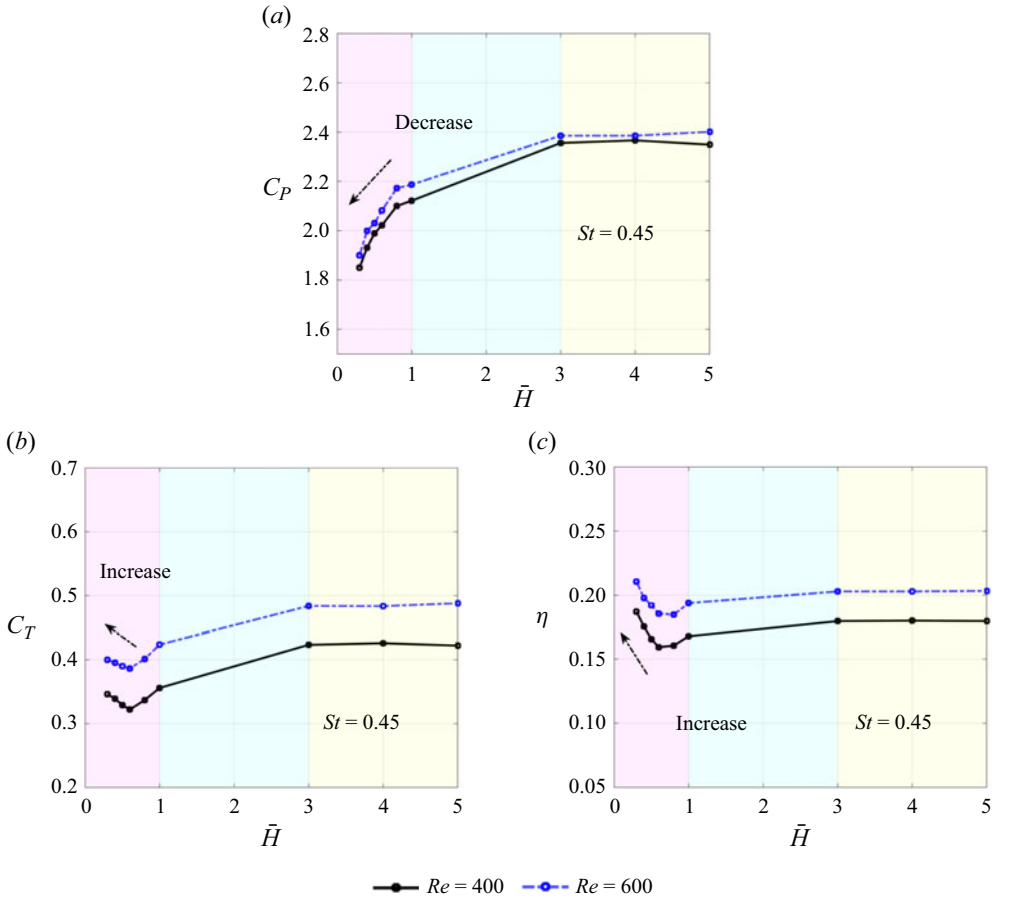


Figure 10. (*a*) Power input coefficient $C_P$, (*b*) thrust coefficient $C_T$ and (*c*) efficiency $\eta$ as a function of the dimensionless submergence depth $\bar{H}$ with $Re = 400$ and $Re = 600$. Here $Fr$ is fixed at 0.6 and $St$ is fixed at 0.45. The overarching pattern observed for $Re = 200$ remains comparable to the outcomes obtained for $Re = 400$ and $Re = 600$.

free surface, resulting in an overall enhancement in efficiency. The uniformity observed across various $Re$ values suggests that the mechanism influencing the enhanced propulsive performance of the flapping plate in the previous sections remains valid within the explored $Re$ range. Further investigation into even higher $Re$ regimes is warranted to comprehensively understand the $Re$ dependence, especially in the context of real-world applications where $Re$ tends to be significantly higher.

## 6. Concluding remarks

In summary, we have employed a two-fluid coupled immersed boundary method to investigate the ground effect of a flapping plate near a free surface. We observe that when $Fr$ is small, the free-surface effect is similar to that of a solid boundary, where both the input power and thrust increase while the efficiency remains constant. However, we have discovered a new type of ground effect caused by the streamlined surface shape and decreased added mass when the surface deformation is significant, leading to decreased power input and increased efficiency. We have also analysed data from the literature on



https://doi.org/10.1017/jfm.2024.830 Published online by Cambridge University Press

real swimmers and found that their *Fr* values are consistent with the optimal *Fr* value of 0.6 that we have determined in our simulations. Although our model is simple, we find that it provides a fundamental framework for understanding the ground effect originating from a free surface.

In reality, fins from aquatic animals are not always oriented vertically (most aquatic mammals), with many instances featuring horizontal orientations (most fish). We aim to delve deeper into understanding this phenomenon, exploring dependencies on Reynolds numbers to much higher ones and three-dimensional effects in future studies. Finally, we remark that in this study, the parameter space is investigated by varying one dimensionless parameter while keeping the other dimensionless parameters fixed. Because the computational costs of the simulation are high, only a limited number of parameter values are simulated. After computing power has a substantial increase in the future, more extensive combinations in the parameter space should be studied to obtain insights into the biological systems in nature.

**Acknowledgements.** We thank Daniel B. Quinn and Keith W. Moored for helpful discussions. L.S. was supported by the University of Minnesota. We also thank the HPC systems of Max Planck Computing and Data Facility (MPCDF) for the allocation of computational time.

**Funding.** We gratefully acknowledge financial support from the Max Planck Society, the German Research Foundation (DFG) from grants 521319293, 540422505 and 550262949 and the Daimler and Benz Foundation.

**Declaration of interests.** The authors report no conflict of interest.

**Author ORCIDs.**
Sida He https://orcid.org/0000-0003-0849-6592;
Xizeng Zhao https://orcid.org/0000-0002-1392-139X;
Lian Shen https://orcid.org/0000-0003-3762-3829;
Xiaojue Zhu https://orcid.org/0000-0002-7878-0655.

## References

Aju, E.J., Gong, P., Pham, D.T., Kaushik, K. & Jin, Y. 2022 On the wake dynamics and thrust generation of a foil flapping over solid and sedimentary beds. *Exp Fluids* **63** (1), 1–11.

Bandyopadhyay, P.R. 2002 Maneuvering hydrodynamics of fish and small underwater vehicles. *Integr. Comput. Biol.* **42** (1), 102–117.

Berke, A.P., Turner, L., Berg, H.C. & Lauga, E. 2008 Hydrodynamic attraction of swimming microorganisms by surfaces. *Phys. Rev. Lett.* **101** (3), 038102.

Blake, R.W. 1979 The energetics of hovering in the mandarin fish (synchropus picturatus). *J. Expl Biol.* **82** (1), 25–33.

Blake, R.W. 1983 Mechanics of gliding in birds with special reference to the influence of the ground effect. *J. Biomech.* **16** (8), 649–654.

Blevins, E. & Lauder, G.V. 2013 Swimming near the substrate: a simple robotic model of stingray locomotion. *Bioinspir. Biomim.* **8** (1), 016005.

Brennen, C.E. 1982 A review of added mass and fluid inertial forces. *Tech. Rep.* CR, 82.010.

Calderer, A., Guo, X., Shen, L. & Sotiropoulos, F. 2018 Fluid–structure interaction simulation of floating structures interacting with complex, large-scale ocean waves and atmospheric turbulence with application to floating offshore wind turbines. *J. Comput. Phys.* **355**, 144–175.

Chung, M.-H. 2016 Propulsive performance of a flapping plate near a free surface. *J. Fluids Struct.* **65**, 411–432.

Coulliette, C. & Plotkin, A. 1996 Aerofoil ground effect revisited. *Aeronaut. J.* **100** (992), 65–74.

Dai, L., He, G. & Zhang, X. 2016 Self-propelled swimming of a flexible plunging foil near a solid wall. *Bioinspir. Biomim.* **11** (4), 046005.

Davenport, J. 1994 How and why do flying fish fly? *Rev. Fish Biol. Fish.* **4** (2), 184–214.

Deng, J., Wang, S., Kandel, P. & Teng, L. 2022 Effects of free surface on a flapping-foil based ocean current energy extractor. *Renew. Energy* **181**, 933–944.



https://doi.org/10.1017/jfm.2024.830 Published online by Cambridge University Press

DENG, J., ZHANG, L., LIU, Z. & MAO, X. 2019 Numerical prediction of aerodynamic performance for a flying fish during gliding flight. *Bioinspir. Biomim.* **14** (4), 046009.

FERNANDO, J.N., WEYMOUTH, G.D. & RIVAL, D.E. 2020 On the limits of added-mass theory in separated flows and with varying initial conditions. *J. Fluids Struct.* **93**, 102835.

FILIPPAS, E.S. & BELIBASSAKIS, K.A. 2014 Hydrodynamic analysis of flapping-foil thrusters operating beneath the free surface and in waves. *Engng Anal. Bound. Elem.* **41**, 47–59.

GAO, Q., DEANE, G.B. & SHEN, L. 2021 Bubble production by air filament and cavity breakup in plunging breaking wave crests. *J. Fluid Mech.* **929**, A44.

GAO, T. & LU, X.-Y. 2008 Insect normal hovering flight in ground effect. *Phys. Fluids* **20** (8), 087101.

HAN, T., ZHONG, Q., MIVEHCHI, A., QUINN, D.B. & MOORED, K.W. 2024 Revealing the mechanism and scaling laws behind equilibrium altitudes of near-ground pitching hydrofoils. *J. Fluid Mech.* **978**, A5.

HE, S., YANG, Z., SOTIROPOULOS, F. & SHEN, L. 2022 Numerical simulation of interaction between multiphase flows and thin flexible structures. *J. Comput. Phys.* **448**, 110691.

LEE, H.-J., JONG, Y.-J., CHANG, L.-M. & WU, W.-L. 2009 Propulsion strategy analysis of high-speed swordfish. *Trans. Japan Soc. Aeronaut. Space Sci.* **52** (175), 11–20.

LI, G.-J. & LU, X.-Y. 2012 Force and power of flapping plates in a fluid. *J. Fluid Mech.* **712**, 598–613.

MIVEHCHI, A., DAHL, J. & LICHT, S. 2016 Heaving and pitching oscillating foil propulsion in ground effect. *J. Fluids Struct.* **63**, 174–187.

MIVEHCHI, A., ZHONG, Q., KURT, M., QUINN, D.B. & MOORED, K.W. 2021 Scaling laws for the propulsive performance of a purely pitching foil in ground effect. *J. Fluid Mech.* **919**, R1.

PARK, H. & CHOI, H. 2010 Aerodynamic characteristics of flying fish in gliding flight. *J. Expl Biol.* **213** (19), 3269–3279.

QUINN, D.B., LAUDER, G.V. & SMITS, A.J. 2014*a* Flexible propulsors in ground effect. *Bioinspir. Biomim.* **9** (3), 036008.

QUINN, D.B., MOORED, K.W., DEWEY, P.A. & SMITS, A.J. 2014*b* Unsteady propulsion near a solid boundary. *J. Fluid Mech.* **742**, 152–170.

REIJTENBAGH, J., TUMMERS, M.J. & WESTERWEEL, J. 2023 Drag force on a starting plate scales with the square root of acceleration. *Phys. Rev. Lett.* **130** (17), 174001.

ROZHDESTVENSKY, K.V. 2006 Wing-in-ground effect vehicles. *Prog. Aerosp. Sci.* **42** (3), 211–283.

RYU, J., PARK, S.G., KIM, B. & SUNG, H.J. 2016 Flapping dynamics of a flexible propulsor near ground. *Acta Mechanica Sin.* **32** (6), 991–1000.

STOKES, I.A. & LUCAS, A.J. 2021 Wave-slope soaring of the brown pelican. *Mov. Ecol.* **9** (1), 1–13.

SUSSMAN, M. & PUCKETT, E.G. 2000 A coupled level set and volume-of-fluid method for computing 3D and axisymmetric incompressible two-phase flows. *J. Comput. Phys.* **162** (2), 301–337.

TANG, C., HUANG, H., GAO, P. & LU, X.-Y. 2016 Self-propulsion of a flapping flexible plate near the ground. *Phys. Rev.* E **94** (3), 033113.

WEBB, P.W. 1993 The effect of solid and porous channel walls on steady swimming of steelhead trout *Oncorhynchus Mykiss*. *J. Expl Biol.* **178** (1), 97–108.

WEBB, P.W. 2002 Kinematics of plaice, *Pleuronectes platessa*, and cod, *Gadus morhua*, swimming near the bottom. *J. Expl Biol.* **205** (14), 2125–2134.

WU, J., QIU, Y.L., SHU, C., ZHAO, N. & WANG, X. 2015 An adaptive immersed boundary-lattice boltzmann method for simulating a flapping foil in ground effect. *Comput. Fluids* **106**, 171–184.

YANG, Z., DENG, B.-Q. & SHEN, L. 2018 Direct numerical simulation of wind turbulence over breaking waves. *J. Fluid Mech.* **850**, 120–155.

ZHONG, Q., HAN, T., MOORED, K.W. & QUINN, D.B. 2021 Aspect ratio affects the equilibrium altitude of near-ground swimmers. *J. Fluid Mech.* **917**, A36.

ZHU, B., CHENG, W., GENG, J. & ZHANG, J. 2022 Energy-harvesting characteristics of flapping wings with the free-surface effect. *J. Renew. Sustain. Energy* **14** (1), 014501.

https://doi.org/10.1017/jfm.2024.830 Published online by Cambridge University Press